# Solution of Incompressible Flow Equations with Physics and Equality Constrained Artificial Neural Networks

D Qifeng Hua, D Inanc Senocak a

<sup>a</sup>Department of Mechanical Engineering and Materials Science, University of Pittsburgh, PA 15261, USA

#### Abstract

We present a meshless method for the solution of incompressible Navier–Stokes equations in advection-dominated regimes using physics- and equality-constrained artificial neural networks combined with a conditionally adaptive augmented Lagrangian formulation. A single neural network parameterizes both the velocity and pressure fields, and is trained by minimizing the residual of a Poisson's equation for pressure, constrained by the momentum and continuity equations, together with boundary conditions on the velocity field. No boundary conditions are imposed on the pressure field aside from anchoring the pressure at a point to prevent its unbounded development. The training is performed from scratch without labeled data, relying solely on the governing equations and constraints. To enhance accuracy in advectiondominated flows, we employ a single Fourier feature mapping of the input coordinates. The proposed method is demonstrated for the canonical lid-driven cavity flow up to a Reynolds number of 7,500 and for laminar flow over a circular cylinder with inflow-outflow boundary conditions, achieving excellent agreement with benchmark solutions. We further compare the present formulation against alternative objective-function constructions based on different arrangements of the flow equations, thereby highlighting the algorithmic advantages of the proposed formulation centered around the Poisson's equation for pressure.

Keywords: Augmented Lagrangian method, constrained optimization, incompressible flow, PECANN, Navier-Stokes equations

#### 1. Introduction

Simulation of high–Reynolds-number incompressible flows over complex geometries has long been a central focus of computational fluid dynamics. Numerous schemes based on finite-difference and finite-volume discretizations have been developed and widely applied to both canonical and industrial flow configurations. These approaches differ fundamentally from methods designed for high-speed compressible flows. Their success hinges critically on enforcing a divergence-free velocity field through the solution of a Poisson equation for the pressure or a pressure-correction variable. An equation for pressure can be derived by taking the divergence of the momentum equations and forcing the velocity field to be

<sup>\*</sup>corresponding author: senocak@pitt.edu (Inanc Senocak)

Email address: qih56@pitt.edu (D Qifeng Hu)

solenoidal. Although a streamfunction–vorticity formulation can bypass the need to calculate pressure field explicitly, such formulations are practically limited to two-dimensional flows. Consequently, most three-dimensional solvers employ the primitive-variable form of the Navier–Stokes equations.

One of the early approaches to solve the incompressible flow equations is the Marker-and-Cell (MAC) method of Harlow and Welch [1] and the projection method introduced indepedently by Chorin [2] and Témam [3]. Both methods uses a Poisson's equation for pressure to enforce incompressibility and prevent the accumulation of divergence errors during time marching. Some of the difficulties of imposing boundary conditions in the MAC method was later addressed with the introduction of the simplified MAC (SMAC) method [4]. In the projection method, an intermediate velocity is first computed without pressure and then projected onto a divergence-free field, producing a splitting error in time. Kim and Moin [5] proposed the fractional step method that improves upon the time-splitting error of the projection method by carefully formulating the boundary conditions on the intermediate velocity field. A comprehensive analysis of different implementations of the projection methods and their implications on numerical accuracy can be found in Guermond et al. [6].

Projection type methods solve the Navier-Stokes equations through a time-marching method. Pressure-based, iterative methods were developed to efficiently compute the steady-state solution of practical flow problems. The Semi-Implicit Method for Pressure-Linked Equations (SIMPLE) [7] was developed, where the advective and diffusive terms in the momentum equations are discretized implicitly. A pressure correction equation is derived and solved to correct the velocity and pressure fields iteratively and through underrelaxation for stability purposes. Several variants of SIMPLE [8, 9, 10] were subsequently introduced to improve its convergence rate and stability. Among them, the Pressure-Implicit with Split Operator (PISO) algorithm [10] extends the SIMPLE methodology to unsteady flows by employing two-stage correction to enforce continuity at each time step without requiring iterations. In the context of spectral element methods, splitting methods were developed to solve the incompressible flow equations [11, 12, 13] and have been adopted in open-source solvers effectively [14, 15].

Physics-informed neural networks (PINNs) have re-emerged as an alternative to conventional mesh-based numerical methods for solving partial differential equations (PDEs). Numerous enhancements to the PINN framework have been proposed to improve its accuracy and extend its applicability to more challenging PDEs. Although training PINNs is typically much slower than using traditional numerical schemes, their main appeal lies in their ability to efficiently solve ill-conditioned inverse PDE problems in a data-driven manner. Consequently, despite their computational cost for forward problems, it is important to demonstrate that PINNs can reliably solve a broad class of PDEs in forward mode without labeled data before deploying them for inverse problems.

PINNs have been applied, with limited success, to the incompressible form of the Navier–Stokes equations. Here, we focus on studies that adopt velocity–pressure formulations. Jin et al. [16] introduced Navier–Stokes flow nets (NSFnets), exploring both velocity–pressure (V–P) and vorticity–velocity (V–V) formulations. While NSFnets can reproduce solutions for low–Reynolds-number flows, they require initial and boundary conditions obtained from analytical solutions or high-fidelity simulations. For example, in the flow over a cylinder, only the two-dimensional wake region was considered, with all inflow around the cylinder

and initial data prescribed from a reference numerical simulation. Despite this, the learned solution agreed with reference solution qualitatively. For turbulent channel flow, due to the computational expense of training neural networks, only a subdomain of the channel was modeled, with DNS data used to supply initial and boundary conditions, and the method was demonstrated for its potential to sustain turbulence. Moreover, although the V–P and V–V formulations yielded comparable accuracy for laminar flows, the V–V formulation produced inconsistent results for the turbulent channel case. NSFnets also benefit from transfer learning, in which a network trained at low Reynolds number is repurposed for higher Reynolds number.

Eivazi et al. [17] used the PINN framework to solve incompressible RANS equations without any specific closure model or assumption for turbulence. However, the network was trained in a supervised fashion using reference DNS data on pressure and velocity on the domain boundaries, including Reynolds-stress components.

McDevitt et al. [18] used PINNs and tested the velocity-pressure and streamfunction-pressure formulations of the incompressible flow equations while enforcing all boundary conditions exactly through a hard-mask. In the case of the well-known lid-driven cavity benchmark problem, velocity-pressure formulation failed to produced acceptable results beyond a Reynolds number of 400. Whereas the streamfunction-pressure formulation produced good results for Reynolds number as high as 5000. This stark difference in performance at high-Reynolds number cases points to the importance of enforcing a divergence-free condition when using the PINN approach. The streamfunction-pressure formulation, albeit limited to 2D flows, enforces the divergence-free condition by design. McDevitt et al. [18] also showed that velocity-pressure formulation can produce good results at higher Reynolds number if supplemental data from a high-fidelity simulation are introduced inside the domain boundaries to train the PINNs.

Recent studies with enhanced network architectures have improved the accuracy of PINNs for incompressible flows at higher Reynolds numbers. Wang et al. [19] introduced the physics-informed residual adaptive network (PirateNet) and simulated lid-driven cavity flow up to Re=3200 using a primitive-variable formulation, reporting excellent agreement with benchmark data. However, their approach required a curriculum training strategy in which the Reynolds number was gradually increased (Re=100,400,1000,1600,3200), significantly raising the computational cost of reaching higher Reynolds numbers.

Wang et al. [20] further employed PirateNets in combination with causality training [21], modern optimization techniques [22], and exact enforcement of boundary conditions as hard constraints to simulate three-dimensional turbulent channel flow at a friction Reynolds number of 395. In this formulation, reference DNS data were used as initial conditions, and turbulence was maintained over a finite time interval. While the resulting mean velocity profile shows excellent agreement with DNS, the mean Reynolds stress components exhibit noticeable discrepancies, particularly near their peak values, indicating remaining limitations in capturing higher-order statistics. Additionally, energy spectra for all velocity components exhibit systematically lower energy across the resolved wavenumber range compared to the DNS spectra, indicating undesirable dissipation in the learned solutions.

The aforementioned studies, despite their limitations, clearly highlight the potential of neural-network-based solvers for incompressible flows and point to an opportunity to further improve the enforcement of the divergence-free condition and boundary conditions. We contend that the standard PINN formulation—where loss terms associated with the governing

equations, boundary and initial conditions, and data are combined into a single composite objective—can only partially enforce these constraints. This observation motivates a more rigorous constrained optimization perspective, rather than a purely multi-objective one, in designing the training objective for neural networks.

In this spirit, we adopt the physics and equality constrained artificial neural networks (PECANN) framework [23], coupled with an augmented Lagrangian method [24, 25] and a conditionally adaptive penalty update strategy recently proposed by Hu et al. [26]. Realizing the importance of hydrodynamic nature of pressure that arise from the conservation of mass principle, we propose a special formulation of the objective function. In our method, a single neural network parameterizes the velocity and pressure field. The residual form of the pressure equation is then constrained by the steady-state momentum and continuity equations, together with the boundary conditions imposed on the momentum field. No boundary conditions are prescribed for the pressure, even in general inflow-outflow configurations. For high–Reynolds-number flows, we incorporate a single layer of Fourier feature mappings to enhance the expressive power of the multilayer perceptron (MLP) representation. In addition, we introduce an adaptive artificial-entropy-viscosity mechanism to stabilize the optimization process; this artificial viscosity is applied only during the early stages of training and has no effect on the converged solution. We demonstrate the efficacy of our proposed method by simulating the lid-driven cavity flow up to a Reynolds number of 7500 and steady flow over a cylinder at a Reynolds number of 40 with general inflow-outflow boundary conditions imposed on the momentum field. Our results show excellent agreement with benchmark data and other published works.

# 2. Methodology

Incompressible flows in the spatio-temporal domain  $\mathcal{U} = \Omega \times [0, T]$  are governed by the Navier-Stokes equations together with the continuity equation:

$$\mathcal{F}(\boldsymbol{x},t) = \frac{\partial \boldsymbol{u}}{\partial t} + (\boldsymbol{u} \cdot \nabla)\boldsymbol{u} + \nabla p - \nu \nabla^2 \boldsymbol{u} = 0 \qquad \text{in } \mathcal{U}, \tag{1a}$$

$$\mathcal{M}(\boldsymbol{x},t) = \nabla \cdot \boldsymbol{u} = 0$$
 in  $\mathcal{U}$ . (1b)

Here,  $\mathbf{x} = [x, y, z]^T$  denotes the spatial coordinate vector and t the time variable. The velocity field is  $\mathbf{u}(\mathbf{x}, t) = [u, v, w]^T$  defined over the spatial domain  $\Omega$  and time interval [0, T], while  $p(\mathbf{x}, t)$  is the pressure field. The kinematic viscosity is  $\nu = 1/Re$ , where Re denotes the Reynolds number. The operator  $\mathcal{F} = [\mathcal{F}_u, \mathcal{F}_v, \mathcal{F}_w]^T$  in Eq. (1a) represents the three components of the momentum conservation equations. The operator  $\mathcal{M}$  in Eq. (1b) enforces the divergence-free condition characteristic of incompressible flows.

These governing equations are supplemented with boundary conditions imposed on the domain boundary  $(\boldsymbol{x},t) \in \partial \mathcal{U}$ , typically expressed in terms of Dirichlet or Neumann operators:

$$\mathcal{D}(\boldsymbol{x},t) = \phi(\boldsymbol{x},t) - g(\boldsymbol{x},t) = 0 \qquad \text{on} \quad \partial_D \mathcal{U},$$
 (2a)

$$\mathcal{N}(\boldsymbol{x},t) = \frac{\partial \phi(\boldsymbol{x},t)}{\partial \boldsymbol{n}} - h(\boldsymbol{x},t) = 0 \qquad \text{on } \partial_N \mathcal{U},$$
 (2b)

where  $\phi$  represents any components of velocity field,  $\boldsymbol{n}$  is the outward normal vector, and  $\partial_D \Omega$  and  $\partial_N \Omega$  denote Dirichlet and Neumann boundaries, respectively. In practice, Dirichlet conditions prescribe the dependent variable directly through  $g(\boldsymbol{x},t)$ , while Neumann conditions impose its normal derivative or flux  $h(\boldsymbol{x},t)$ . For fluid flows, typical examples include no-slip walls with zero velocity, slip walls with prescribed tangential velocity, velocity inlets with given profiles. Although, we test Dirichlet and Neumann type boundary conditions on the pressure field, our proposed method can learn flow solution without imposing any boundary conditions on the pressure field. However, pressure is constrained to an arbitrary fixed value at a single collocation point to prevent its unbounded growth.

Although, our current focus is on steady-state flows, for time-dependent problems, additional initial conditions must be specified on the initial domain  $\Gamma = \Omega \times \{t = 0\}$ , typically expressed using Dirichlet operators:

$$\mathcal{I}_{\phi}(\boldsymbol{x},t) = \phi(\boldsymbol{x},t) - \phi_0(\boldsymbol{x}) = 0 \quad \text{in} \quad \Gamma,$$
(3)

where  $\phi_0(\mathbf{x})$  denotes the prescribed initial distribution of the field  $\phi$  at t=0.

As discussed in the Introduction section, the technical challenge to numerically solve the incompressible form of the Navier-Stokes equations in primitive variables is the lack the simultaneous determination of velocity and pressure remains challenging. The velocity field is governed by its own momentum equations, but the pressure lacks an independent governing equation. In contrast to compressible flows, where pressure is coupled to density and temperature through an equation of state as a thermodynamic quantity, incompressible formulations require an alternative treatment for pressure due its hydrodynamic nature. A common approach is to derive a Poisson equation for pressure by taking the divergence of the momentum equations and requiring the velocity field to be solenoidal (divergence-free):

$$\mathcal{P}(\boldsymbol{x}) = \nabla^2 p + (\nabla \boldsymbol{u}) : (\nabla \boldsymbol{u})^\top = 0 \text{ in } \mathcal{U}.$$
 (4)

Since Eq. (4) is strictly conditioned on the satisfaction of the governing equations (1) due a solenoidal velocity field, we propose a pressure-based equality-constrained optimization problem for learning incompressible flows by a single neural network parameterized by  $\theta$  to approximate the true velocity and pressure fields without splitting the momentum equations:

$$[\hat{\boldsymbol{u}}, \hat{p}]^T(\boldsymbol{x}, t; \theta) \approx [\boldsymbol{u}, p]^T.$$
 (5)

In this formulation, the averaged residual of the pressure Poisson equation is adopted as the objective function  $\mathcal{J}$ , while the momentum equations with the pressure gradient terms are enforced separately as equality constraints  $\mathcal{C}_{Fk}$  ( $k \in u, v, w$ ), along with the conservation of mass principle, which requires the velocity field to be solenoidal  $\mathcal{C}_M$ , boundary conditions  $\mathcal{C}_{D_j}$ ,  $\mathcal{C}_{N_j}$ , and initial conditions  $\mathcal{C}_{I\phi}$ . These loss terms are expressed in terms of mean-squared

errors as follows:

$$\min_{\theta} \quad \mathcal{J}(\theta; \boldsymbol{x}, t) = \frac{1}{N_{\mathcal{U}}} \sum_{i=1}^{N_{\mathcal{U}}} \|\mathcal{P}(\theta; \boldsymbol{x}_{i}, t_{i})\|_{2}^{2} \qquad \text{in} \quad \mathcal{U},$$
subject to  $C_{Fk}(\theta; \boldsymbol{x}, t) = \frac{1}{N_{\mathcal{U}}} \sum_{i=1}^{N_{\mathcal{U}}} \|\mathcal{F}_{k}(\theta; \boldsymbol{x}_{i}, t_{i})\|_{2}^{2} = 0 \quad \text{in} \quad \mathcal{U},$ 

$$C_{M}(\theta; \boldsymbol{x}, t) = \frac{1}{N_{\mathcal{U}}} \sum_{i=1}^{N_{\mathcal{U}}} \|\mathcal{M}(\theta; \boldsymbol{x}_{i}, t_{i})\|_{2}^{2} = 0 \quad \text{in} \quad \mathcal{U},$$

$$C_{D_{j}}(\theta; \boldsymbol{x}, t) = \frac{1}{N_{D_{j}}} \sum_{i=1}^{N_{D_{j}}} \|\mathcal{D}(\theta; \boldsymbol{x}_{i}, t_{i})\|_{2}^{2} = 0 \quad \text{on} \quad D_{j} \subseteq \partial_{D}\mathcal{U},$$

$$C_{N_{j}}(\theta; \boldsymbol{x}, t) = \frac{1}{N_{N_{j}}} \sum_{i=1}^{N_{N_{j}}} \|\mathcal{N}(\theta; \boldsymbol{x}_{i}, t_{i})\|_{2}^{2} = 0 \quad \text{on} \quad N_{j} \subseteq \partial_{N}\mathcal{U},$$

$$C_{I_{\phi}}(\theta; \boldsymbol{x}, t) = \frac{1}{N_{I}} \sum_{i=1}^{N_{I}} \|\mathcal{I}_{\phi}(\theta; \boldsymbol{x}_{i}, t_{i})\|_{2}^{2} = 0 \quad \text{on} \quad \Gamma.$$
(6)

Here,  $j \in \{u, v, \frac{\partial u}{\partial n}, p, \dots\}$  enumerates the boundary segments. This proposed formulation thus provides a physics-consistent metric of performance, where the objective value directly measures how well the pressure field satisfies the Poisson's equation, while the constraints guarantee adherence to independent momentum and mass conservation, and prescribed conditions.

Employing the conditionally adaptive augmented Lagrangian method (CA-ALM) [26], the constrained optimization problem is reformulated as an unconstrained one with constraint-specific penalty parameters:

$$\max_{\lambda} \min_{\theta} \mathcal{L}(\theta, \lambda; \mu) = \mathcal{J}(\theta) + \lambda^{T} \mathcal{C}(\theta) + \frac{1}{2} \mu^{T} [\mathcal{C}(\theta) \odot \mathcal{C}(\theta)], \tag{7}$$

where  $\mathcal{C}(\theta)$  collects all constraints into a vector,  $\odot$  denotes the elementwise (Hadamard) product,  $\lambda$  is the vector of Lagrange multipliers, and  $\mu$  contains the positive penalty parameters, with  $\mu_i$  associated with constraint  $\mathcal{C}_i$ . The complete training procedure for updating  $\theta, \lambda, \mu$  are presented in vectorized form in Algorithm 1.

In Eq. (6), multiple constraints are present, each associated with a penalty scaling factor  $\eta_i \in \boldsymbol{\eta}$  in Alg. 1, typically chosen from  $10^{-2}, 10^{-1}, 1$ . These factors are used to reflect the relative priority of constraints during optimization. In particular, the scaling factors for the PDE constraints should be chosen smaller than those for data-related constraints, such as boundary and initial conditions. This prioritization ensures that the optimization process first enforces physical satisfaction at the boundaries and initial state before focusing on reducing the residuals of the governing PDEs. In the following experiments, we recommend setting  $\eta_i = 1$  for the boundary and initial conditions, as well as for the continuity constraint  $\mathcal{C}_M$ , while assigning smaller values (e.g.,  $\eta_i = 0.1$ ) to the momentum equations.

```
Algorithm 1: Conditional Adaptive Augmented Lagrangian method (CA-ALM) [26]
```

```
1 Defaults: \zeta = 0.99, \ \omega = 0.999, \ \epsilon = 10^{-16}
  2 Input: \theta^0, E, \eta
  з oldsymbol{\lambda}^0=\mathbf{1}
                                                        /* Initializing Lagrange multipliers
                                                                                                                                                                              */
  4 \mu^0 = 1
                                                        /* Initializing penalty parameters
  5 \ \bar{\mathbf{v}}^0 = \mathbf{0}
                                                        /* Initializing averaged square-gradients
                                                                                                                                                                              */
  6 \mathcal{L}^0 = \infty
                                                      /* Initializing augmented Lagrangian loss
  7 for e = 1 to E... do
             \theta^e \leftarrow \text{Update}(\theta^{e-1})
                                                                                                     /* primal update
             \mathcal{L}^e \leftarrow \text{Eq. 7} \text{ with } \theta^e, \boldsymbol{\lambda}^{e-1}, \boldsymbol{\mu}^{e-1}, \cdots
                                                                                                     /* augmented loss update
  9
                                                                                                                                                                              */
             \bar{\mathbf{v}}^e \leftarrow \zeta \ \bar{\mathbf{v}}^{e-1} + (1-\zeta) \ (\mathcal{C}(\theta^e) \odot \mathcal{C}(\theta^e))
                                                                                                   /* square-gradient update
10
            \begin{array}{l} \textbf{if } \mathcal{L}^e \geq \omega \mathcal{L}^{e-1} \textbf{ then} \\ \mid \quad \boldsymbol{\lambda}^e \leftarrow \boldsymbol{\lambda}^{e-1} + \boldsymbol{\mu}^{e-1} \odot \boldsymbol{\mathcal{C}}(\theta^e) \end{array}
11
                                                                                                         /* dual update
12
                 oldsymbol{\mu}^e \leftarrow \max\left(oldsymbol{\mu}^{e-1}, rac{oldsymbol{\eta}}{\sqrt{ar{\mathbf{v}}^e + \epsilon}}
ight)
13
                                                                                                                                                                              */
14 end
15 Output: \theta^E
```

## 2.1. Baseline formulation

To enable comparison with the proposed pressure-based formulation of the objective function (6), we also construct a baseline equality-constrained optimization problem that does not involve the pressure Poisson equation. In this simpler formulation, the objective  $\mathcal{J}_b$  is to minimize the cumulative momentum losses  $\mathcal{C}_{Fk}$ , while all other constraints in Eq. (6) are still enforced:

$$\min_{\theta} \quad \mathcal{J}_b(\theta; \boldsymbol{x}, t) = \sum_{k} \mathcal{C}_{Fk}(\theta; \boldsymbol{x}, t) \qquad \text{in} \quad \mathcal{U},$$
subject to 
$$\boldsymbol{\mathcal{C}}(\theta) = \left[\mathcal{C}_M(\theta; \boldsymbol{x}, t), \mathcal{C}_{D_j}(\theta; \boldsymbol{x}, t), \mathcal{C}_{N_j}(\theta; \boldsymbol{x}, t), \mathcal{C}_{I_{\phi}}(\theta; \boldsymbol{x}, t)\right]^T = \mathbf{0}.$$
(8)

In practice, reducing the coupled momentum losses in the objective necessitates careful increases of the Lagrange multipliers and penalty parameters in the ALM. The baseline formulation requires significantly smaller penalty scaling factors to achieve stable and accurate predictions; here, they are set to 0.01 times those used in the proposed formulation.

### 2.2. Adaptive, vanishing entropy viscosity

High-order numerical schemes are prone to numerical instability when applied to advection-dominated flows characterized by large Reynolds numbers. A common remedy is to introduce an artificial viscosity term, such that the effective viscosity becomes

$$\nu = \frac{1}{Re} + \nu_a,\tag{9}$$

thereby relaxing the near-zero diffusion regime [27, 28].

In the context of PINNs, Shukla et al. [29] employed a global artificial entropy viscosity in a linear form

$$\nu_a^l = \min\left(\beta \frac{1}{Re}, \alpha \frac{L^2}{U_\infty^2} ||r||_\infty\right),\tag{10}$$

where the entropy residual r was estimated following [30]:

$$r = (\boldsymbol{u} - \boldsymbol{u}_m) \cdot \mathcal{F}(x, t). \tag{11}$$

Here,  $\beta$  and  $\alpha$  are prescribed constants that govern the initial magnitude and decay rate of the artificial viscosity, and L and  $U_{\infty}$  denote characteristic length and velocity scales,  $\boldsymbol{u}_{m}$  represents a reference velocity vector used in defining the entropy residual.

When we adopted this global artificial entropy viscosity formulation in the PECANN framework, we find that predictive performance is highly sensitive to the choice of  $\beta$  and  $\alpha$ .

Realizing the role of artificial entropy viscosity in regularizing the optimization process during the early stages of training, we propose an adaptive, vanishing entropy viscosity  $(\nu_a^a)$  that dynamically adjusts the amount of artificial viscosity based on optimization feedback. Following the same logistics as in CA-ALM (Algorithm 1), we maintain an exponential moving average of the squared entropy norm  $(||r||_{\infty})^2$  and use its unbiased root to update the artificial viscosity  $\nu_a^a$  at epoch e:

$$\kappa^{(e)} \leftarrow \zeta \kappa^{(e-1)} + (1 - \zeta)(||r||_{\infty})^{2},$$

$$\nu_{a}^{a(e)} \leftarrow \min(\nu_{a}^{a(e-1)}, \frac{\sqrt{\kappa^{e}}}{1 - \zeta^{e}}||r||_{\infty}), \text{ if } \nu_{a}^{a(e-1)} > \frac{1}{4Re}, \text{ otherwise } 0.$$
(12)

Here,  $\kappa^{(0)}=1$  is chosen to prevent an initial rapid drop in  $\nu_a^{a(0)}$ , while the unbiased form  $\frac{\sqrt{\kappa^{(e)}}}{1-\zeta^{(e)}}$  avoids  $\nu_a^a$  being artificially large. The initial artificial viscosity is fixed at  $\nu_a^{a(0)}=\frac{1}{200}$ , corresponding to an additional Reynolds number of 200 for all high-Re cases. Once  $\nu_a^a$  falls below  $\frac{1}{4Re}$ , the artificial viscosity is effectively turned off.

## 2.3. Fourier feature mappings

A Fourier feature mapping,  $\gamma$ , projects input coordinates  $\mathbf{x} \in \mathbb{R}^d$  into a higher-dimensional space via sinusoidal transformations, thereby enhancing the expressive capacity of MLPs [31, 32]. This technique is theoretically grounded in Bochner's theorem and can be interpreted as a Fourier approximation of a stationary kernel function [31], enabling the network to more effectively capture high-frequency components in the input space.

A single Fourier feature mapping is defined as:

$$\gamma(\mathbf{x}) = \begin{bmatrix} \cos(2\pi \mathbf{B} \mathbf{x}) \\ \sin(2\pi \mathbf{B} \mathbf{x}) \end{bmatrix}$$
 (13)

where  $\mathbf{B} \in \mathbb{R}^{m \times d}$  consists of entries sampled from a Gaussian distribution  $\mathcal{N}(0, \sigma)$ , which remain fixed during training. The resulting transformed input, considered as the first hidden layer, is then passed to a standard fully connected neural network with L hidden layers, defined by the following layer-wise operations:

$$\mathbf{H}_{1} = \gamma(\mathbf{x}),$$

$$\mathbf{H}_{\ell} = \psi(\mathbf{W}_{\ell} \cdot \mathbf{H}_{\ell-1} + \mathbf{b}_{\ell}), \quad \ell = 2, \dots, H,$$

$$f_{\theta}(\mathbf{x}) = \mathbf{W}_{L+1} \cdot \mathbf{H}_{L} + \mathbf{b}_{L+1},$$
(14)

where  $\theta = \{\mathbf{W}_{\ell}, \mathbf{b}_{\ell}, ...\}$  and  $\psi$  represents the activation function. In the following implementation, the stardard deviation of the Gaussian distribution  $\sigma$  is set to 1.0, following the empirical demonstration of PECANN employing a Fourier net in Hu et al. [26]. Additionally, the conventional MLP architecture is recovered as a special case of (14) with

$$\gamma(\mathbf{x}) = \mathbf{W}_1 \mathbf{x} + \mathbf{b}_1.$$

## 3. Application to internal and external flow scenarios

Given an *n*-dimensional vector of predictions  $\hat{\boldsymbol{u}} \in \mathbf{R}^n$  and an *n*-dimensional vector of exact values  $\boldsymbol{u} \in \mathbf{R}^n$ , we define the relative Euclidean or  $l^2$  norm, infinity norm  $l^{\infty}$  norm, and the root-mean square (RMS), respectively, to assess the accuracy of our predictions

$$\mathcal{E}_r(\hat{u}, u) = \frac{\|\hat{\boldsymbol{u}} - \boldsymbol{u}\|_2}{\|\boldsymbol{u}\|_2}, \quad \mathcal{E}_{\infty}(\hat{u}, u) = \|\hat{\boldsymbol{u}} - \boldsymbol{u}\|_{\infty}, \tag{15}$$

where  $\|\cdot\|_2$  denotes the Euclidean norm, and  $\|\cdot\|_{\infty}$  denotes the maximum norm.

Unless otherwise stated, we use artificial neural networks with hyperbolic tangent activation functions and Xavier initialization scheme [33]. L-BFGS optimizer available in the Pytorch package [34] is employed with *strong Wolfe* line search function. For evaluations involving statistical performance, such as the relative  $l^2$  norm, the mean prediction and its standard deviation are based on five independent trials.

# 3.1. Internal flow example: lid-driven cavity flow

The two-dimensional lid-driven cavity (LDC) flow is a widely used benchmark for assessing numerical methods for incompressible flows. A particular advantage of this configuration is its closed domain, which facilitates stringent verification of mass conservation. For the LDC problem, a key objective is to demonstrate excellent agreement with well-established benchmark data [35, 36] at Reynolds numbers of 1000 and above. When implemented correctly, finite-difference and finite-volume methods combined with projection-type algorithms have demonstrated remarkable success in matching these benchmark solutions with high fidelity. However, it is not uncommon for some numerical methods to perform very well at Re = 100 and Re = 400, yet exhibit significant discrepancies at Re = 1000, highlighting the difficulty of achieving both local and global mass conservation for advection-dominated flow scenarios. To this end, LDC problem is equally challenging for PINNs as well [29]. Motivated by this historical context, we simulate the LDC problem at Reynolds numbers up to 7,500.

In the steady-state regime, the problem is defined in a closed square cavity  $\Omega = \{(x,y)|0 \le x, y \le 1\}$ , where the top lid moves with a prescribed velocity in the x-direction and the remaining walls satisfy no-slip conditions, thus involving only Dirichlet boundary conditions. As the Reynolds number increases, the flow develops characteristic vortices, and the predicted velocity profiles are commonly validated against reference data [35, 36].

Here, we skip the Re = 1000 case and start directly with the more challenging Re = 2500 case to perform a comprehensive ablation study comparing our proposed pressure-based and baseline formulations for the objective function. Two additional design choices are considered: the network architecture (Fourier network or MLP) and the entropy-viscosity

strategy (linear  $\nu_a^l$  or adaptive  $\nu_a^a$ ). We then apply our proposed method to Reynolds number cases of Re=5000 and Re=7500.

Unlike finite-difference methods on a structured Cartesian mesh, the velocity discontinuities at the intersections of the moving lid with the sidewalls generate large, localized residuals that hinder optimizer convergence. To alleviate this issue, a smooth lid velocity profile is adopted following Wang et al. [19]:

$$u(x,1) = 1 - \frac{\cosh[50(x-0.5)]}{\cosh(25)}, \quad v(x,1) = 0.$$
 (16)

Additionally, since only the spatial derivatives of the pressure field appear in the governing equations, the pressure field is anchored to an arbitrary reference value at an arbitrary point within the domain (p(0.5, 0.5) = 0). This point-wise constraint is enforced with its own penalty scaling factor of  $\eta_p = 0.1$ . The constrained optimization problem for the pressure-based formulation is then written as

$$\min_{\boldsymbol{\theta}} \mathcal{J}(\boldsymbol{\theta}; \boldsymbol{x}), \quad \text{subject to} \quad \mathcal{C}(\boldsymbol{\theta}; \boldsymbol{x}) = [\mathcal{C}_{Fu}, \mathcal{C}_{Fv}, \mathcal{C}_{M}, \mathcal{C}_{Bu}, \mathcal{C}_{Bv}, \mathcal{C}_{p}]^{T} = \boldsymbol{0}.$$
 (17)

For comparison, the baseline formulation is expressed as

$$\min_{\theta} \mathcal{J}_b(\theta; \boldsymbol{x}) = \mathcal{C}_{Fu} + \mathcal{C}_{Fv}, \quad \text{subject to} \quad \mathcal{C}(\theta; \boldsymbol{x}) = [\mathcal{C}_M, \mathcal{C}_{Bu}, \mathcal{C}_{Bv}, \mathcal{C}_p]^T = \boldsymbol{0},$$
 (18)

which omits the pressure Poisson equation and directly minimizes the momentum residuals constrained by the boundary conditions on the velocity field, divergence-free condition, and anchoring of the pressure field at a single point.

#### 3.1.1. Ablation study

We employ neural networks with four hidden layers, each containing 80 neurons (for the Fourier net, the first hidden layer corresponds to the Fourier feature mapping). Each model is trained for a total of 100,000 epochs. A total of 20,000 residual points are randomly sampled within the domain, and 256 points are sampled along each boundary. Note that the averaged divergence-free constraint,  $C_M$ , is evaluated over all residual and boundary points. For the global artificial entropy viscosity,  $\nu_a^l$ , (Eq. 10), the characteristic length and velocity are set to L=1 and  $U_{\infty}=1$ , respectively. The reference velocity is defined as  $\mathbf{u}_m=(0.5,0.5)$ , and the prescribed constants  $\beta=5$  and  $\alpha=0.03$  as adopted in [29].

Figure 1 presents the mean and standard deviation (Std. band) of the predicted vertical velocity profiles, v(x,0.5), obtained using different formulations and four combinations of design choices. In Figure 1(a), which corresponds to the baseline formulation, none of the combinations achieves fully accurate predictions. Among them, the Fourier network with  $\nu_a^a$ , adaptive update of entropy viscosity, yields results closest to the reference data. In contrast, the Fourier network with  $\nu_a^l$ , linear update, produces inconsistent mean trends and exhibits a wider deviation band. When employing the proposed pressure-based formulation in Figure 1(b), the overall prediction accuracy is notably improved, except for the previously-mentioned configuration that remains inconsistent. Two configurations deliver the most reliable results—those using  $\nu_a^a$ —regardless of the underlying network architecture. A similar pattern is observed for the horizontal velocity profiles, u(0.5, y), as shown in Figure 2.

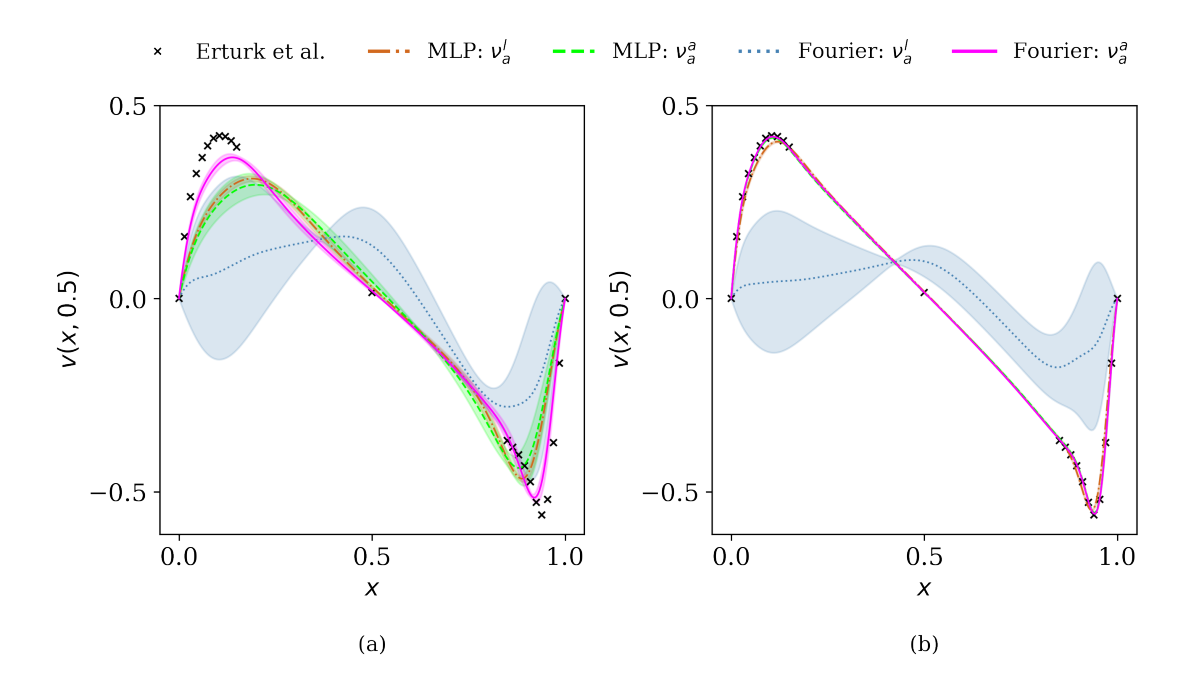


Figure 1: Lid-driven cavity flow at Re = 2500: mean and standard deviation (Std. band) of the predicted v-velocity along y = 0.5 for (a) the baseline formulation (Eq. 8) and (b) the proposed pressure-based formulation (Eq. 6).

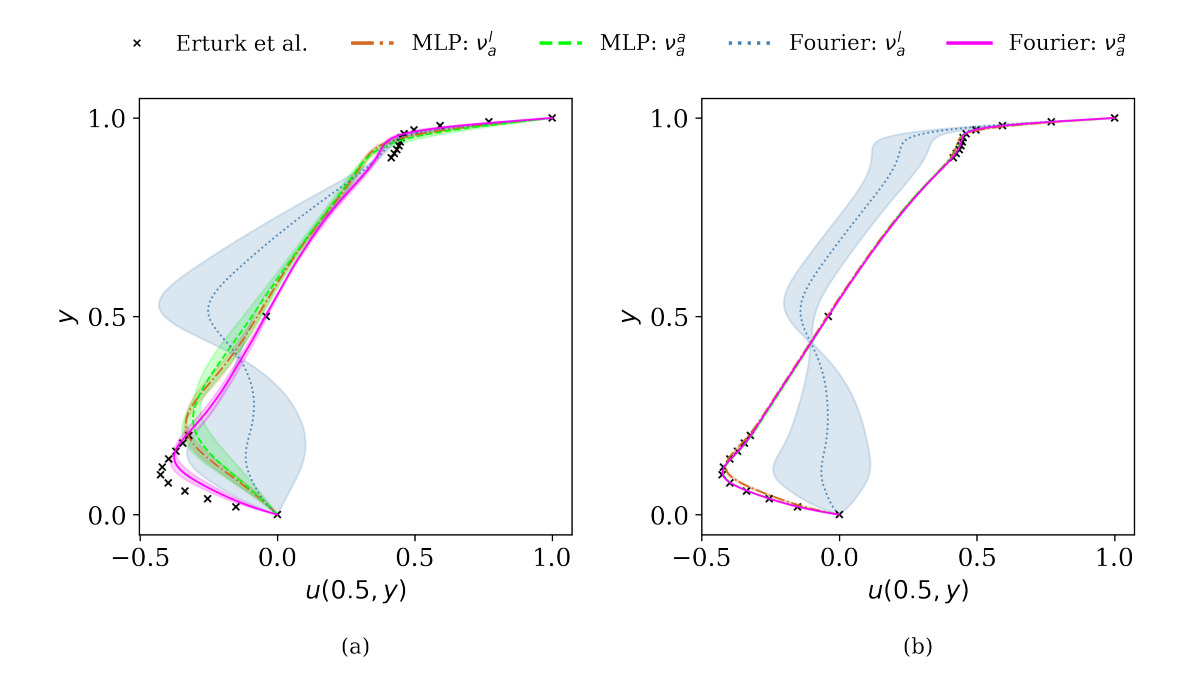


Figure 2: Lid-driven cavity flow at Re = 2500: mean and standard deviation (Std. band) of the predicted u-velocity along x = 0.5 for (a) the baseline formulation (Eq. 8) and (b) the proposed pressure-based formulation (Eq. 6).

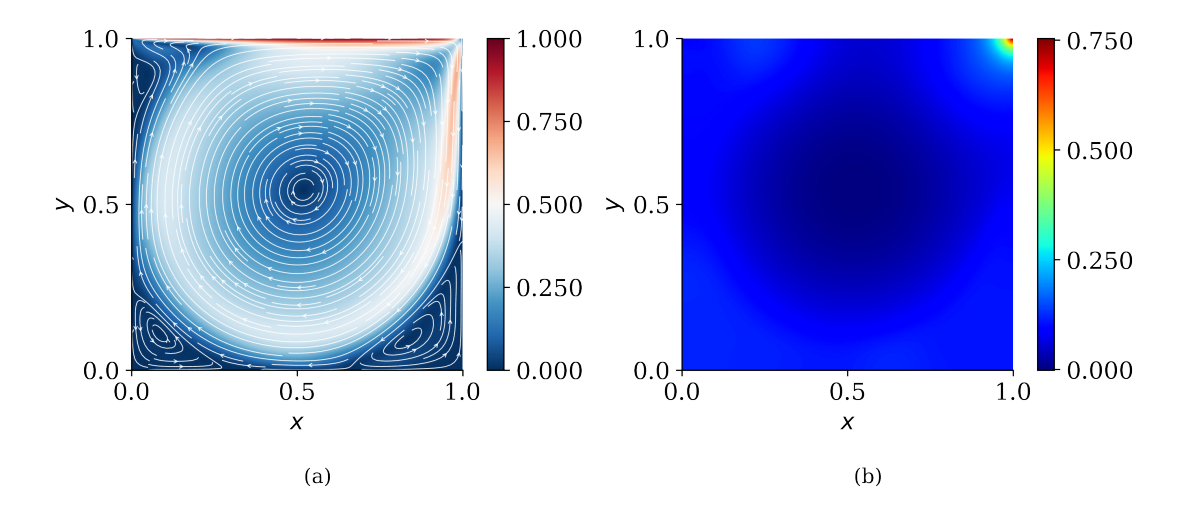


Figure 3: Lid-driven cavity flow at Re=2500: (a) predicted velocity field with streamlines from one trial using adaptive, vanishing entropy viscosity,  $\nu_a^a$ , in the pressure-based formulation, and (b) the corresponding pressure field.

Figure 3 illustrates the predicted velocity field with streamlines and the corresponding pressure distribution from a trial using  $\nu_a^a$ , adaptive update of entropy viscosity, in the pressure-based formulation. In Fig. 3(a), the implementation successfully captures all four vortical structures with closed streamlines, particularly the small fourth vortex near the top-left corner.

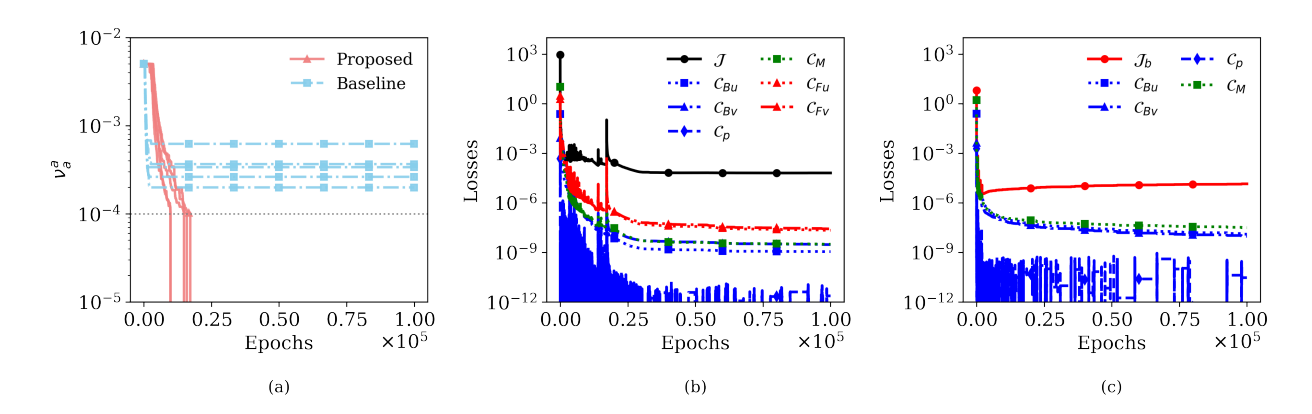


Figure 4: Lid-driven cavity flow at Re=2500: comparison of the training behaviors between the proposed and baseline formulations using the Fourier net with an adaptive, vanishing entropy viscosity,  $\nu_a^a$ . (a) Evolution of  $\nu_a^a$  over epochs for all trials, (b) evolution of the objective and constraint losses from one trial of the proposed formulation, and (c) evolution of the loss terms in the baseline formulation.

To analyze the training behavior of different formulations, we first focus on the configuration, Fourier networks with  $\nu_a^a$ , that yields the closest agreement with the reference data even in the baseline one, as shown in Fig. 1(a) and Fig. 2(a). Using this configuration, we compare the evolution of  $\nu_a^a$  and the corresponding loss terms between the two formulations in Figure 4.

In Fig. 4(a), although the five baseline trials exhibit sharp decreases in  $\nu_a^a$  during the

initial stage, the values soon plateau above the deactivation threshold of  $10^{-4}$ . In contrast, the proposed pressure-based formulation maintains the initial  $\nu_a^a$  for several epochs before exhibiting a gradual decay, reaching the threshold before  $2.5 \times 10^4$  epochs. Figs. 4(b-c) show the corresponding objective and constraint losses from one trial of each formulation. The proposed pressure-based formulation converges at approximately  $4 \times 10^4$  epochs, with the boundary and divergence-free constraints stabilizing around  $10^{-9}$ , indicating near-exact satisfaction. The momentum losses converge to approximately  $10^{-7}$ , while the pressure-Poisson objective stabilizes near  $10^{-4}$ . In contrast, the baseline converges more rapidly but stabilizes at a higher objective value (sum of the momentum losses) exceeding  $10^{-6}$ . Subsequent optimization fails to reduce this further, leaving both the global entropy constant and  $\nu_a^a$  essentially unchanged.

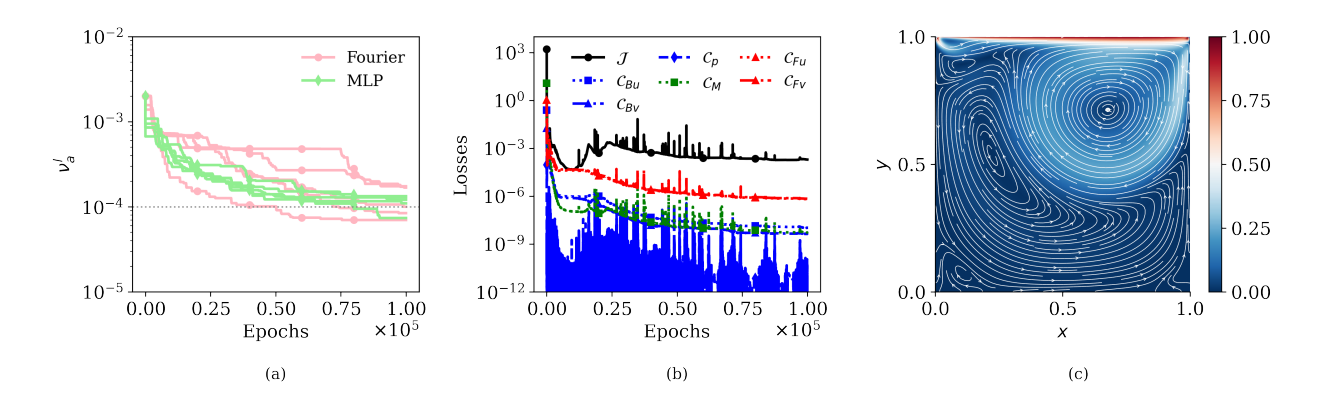


Figure 5: Lid-driven cavity flow at Re = 2500: (a) comparison of linear entropy viscosity  $\nu_a^l$  evolution between the Fourier net and MLP under the pressure-based formulation, (b) evolution of the objective and constraint losses from a Fourier-net trial, and (c) the corresponding predicted velocity field.

Another notable configuration is the Fourier network equipped with the linear artificial viscosity  $\nu_a^l$ , which exhibits inconsistent performance across both formulations, as shown in Figs. 1 and 2. To investigate this degraded behavior, Fig. 5 shows the evolution of  $\nu_a^l$  under the pressure-based formulation, together with the loss history and the predicted velocity field from a representative Fourier-network trial.

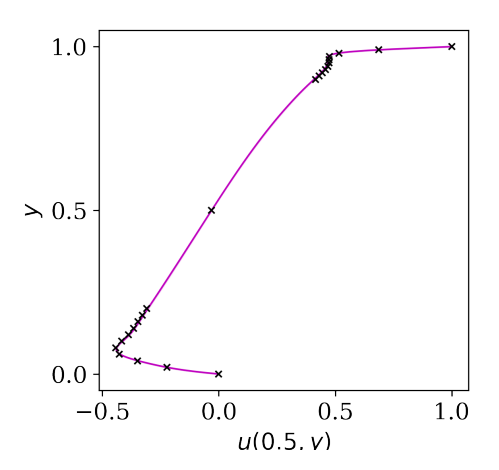
In Fig. 5(a), the linear updates of  $\nu_a^l$  decay much more slowly for both architectures, and few trials reach the deactivation threshold defined in the adaptive scheme, unlike those in Fig. 4(a). Furthermore, the Fourier networks exhibit pronounced inconsistency in the rate of decay compared to the MLPs. This persistent artificial viscosity indeed explains the slight mismatches observed in the MLP velocity profiles in Figs. 1(b) and 2(b), as the increased effective momentum diffusion still impairs the final predictive accuracy. However, this mechanism alone cannot account for the degraded performance observed in the Fourier network.

Fig. 5(b) shows highly fluctuating loss evolution over epochs for one Fourier-net trial, which each spike in the loss curves corresponds to a decrease in  $\nu_a^l$ . The converged loss values are also higher than those observed with adaptive updates in Fig. 4(b), particularly for the momentum constraints, which stabilize around  $10^{-6}$ . The corresponding predicted velocity field in Fig. 5(c) reveals an unexpected circulation pattern in major disagreement with benchmark simulation. Velocity attains values that are very small across most of the domain

except for a localized high-velocity region near the top-right corner. A similar solution with an unexpected circulation pattern was reported in Shukla et al. [29] for Kolmogorov–Arnold networks (KAN) using linear updates of  $\nu_A$ . The underlying mechanism behind this behavior remains unclear. It may be related to the enhanced expressiveness of the network architectures and the initialization of  $\nu_a^l$  through  $\beta/Re$ , which decreases with increasing Reynolds number. While this hypothesis warrants further investigation, a detailed analysis is beyond the scope of the present study.

#### 3.1.2. Reynolds number Re = 5000

Building on the observations from the previous Reynolds-number case, we next consider Re = 5000 using the pressure-based formulation (6) with Fourier feature mapping (14) and adaptive entropy viscosity  $\nu_a^a$  (12). With the same number of collocation points as in the case of Re = 2500, the configuration maintains highly consistent agreement with the reference data of Erturk et al. [36], as shown in Fig. 6.



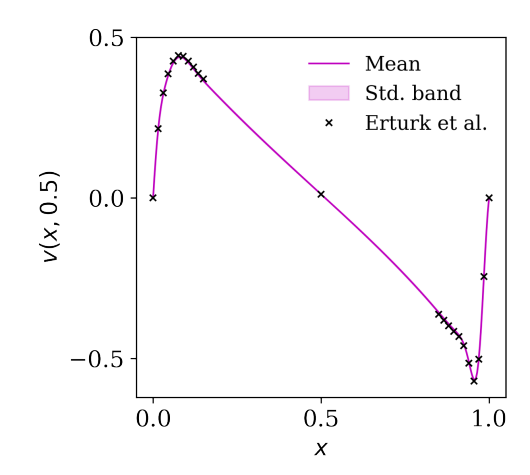


Figure 6: Lid-driven cavity flow at Re = 5000: mean and standard deviation of predicted (a) horizontal velocity u along x = 0.5 and (b) vertical velocity v along y = 0.5, compared to the benchmark data of Erturk et al. [36].

Figure 7(a) shows the predicted velocity field from one trial. At Re = 5000, the prediction accurately captures the larger vortex near the top-left corner, consistent with the expected strengthening of the circulation compared to the Re = 2500 case. However, the smallest secondary vortex near the bottom-right corner is less distinct, in contrast to the presentation of Erturk et al. [36]. Fig. 7(b) presents the corresponding evolution of the objective and constraint terms. The final spike in the loss curve occurs when the adaptive viscosity  $\nu_a^a$  vanishes at approximately  $2 \times 10^4$  epochs, after which the optimization finally stabilizes around  $4 \times 10^4$  epochs.

## 3.1.3. Reynolds number Re = 7500

Further tests with the same configuration at Re = 7500 reveal a slight mismatch in the mean predicted profiles, despite the overall consistency observed in Fig. 8. The enlarged secondary vortex in the bottom-right corner, shown in Fig. 9(a), indicates that the model is still capturing the qualitative evolution of the flow. However, the convergence becomes

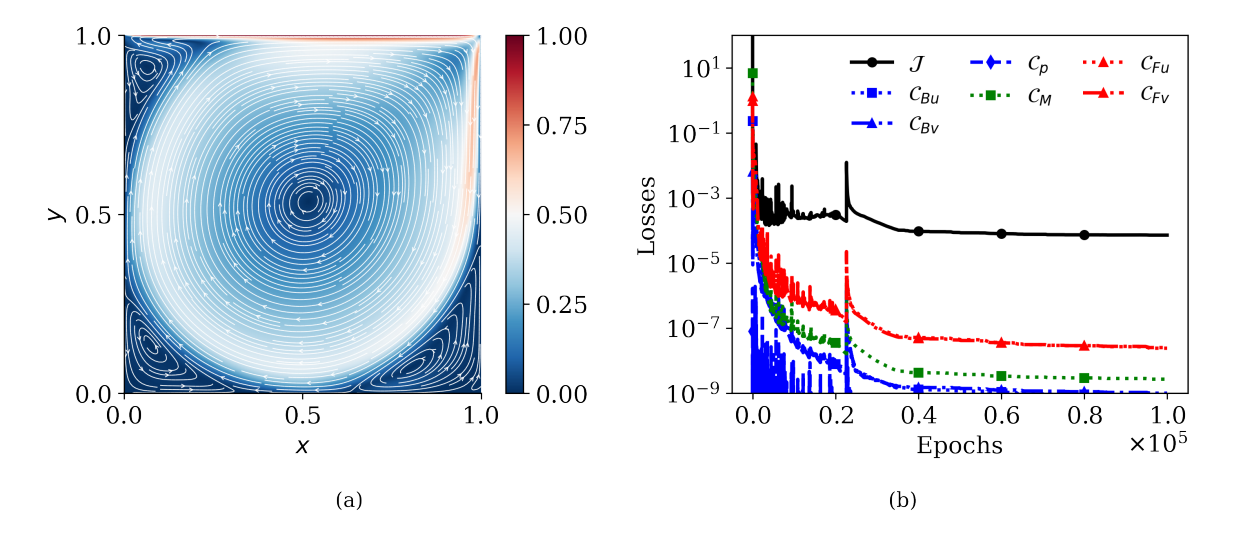


Figure 7: Lid-driven cavity flow at Re = 5000: (a) velocity field with streamlines from one Fourier-network trial with adaptive entropy viscosity; (b) corresponding loss evolution.

noticeably slower: the adaptive artificial viscosity vanishes around  $4 \times 10^4$  epochs, and the subsequent convergence does not occur until approximately  $10^5$  epochs.

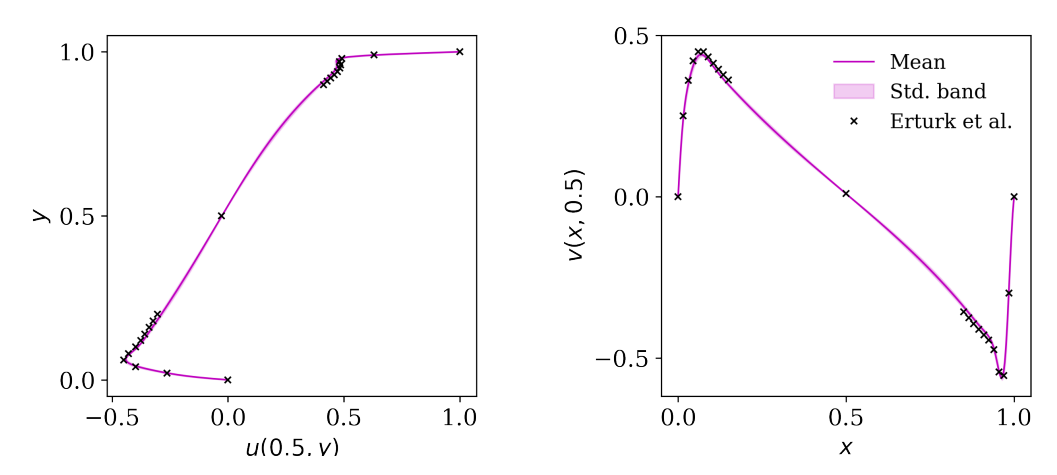


Figure 8: Lid-driven cavity flow at Re = 7500: mean and standard deviation of predicted (a) horizontal velocity u along x = 0.5 and (b) vertical velocity v along y = 0.5, compared to the benchmark data of Erturk et al. [36].

# 3.2. External flow example: steady, laminar flow over a cylinder

This subsection demonstrates that the proposed pressure-based formulation can be readily applied to external flow problems with a general inlet-outlet boundaries. As a canonical example, we consider the two-dimensional laminar flow over a cylinder at Re = 40. This steady-state regime features two symmetric attached vortices behind the cylinder, and key quantities such as the drag coefficient, separation angle, and wake length are used to validate the accuracy of the predictions [37].

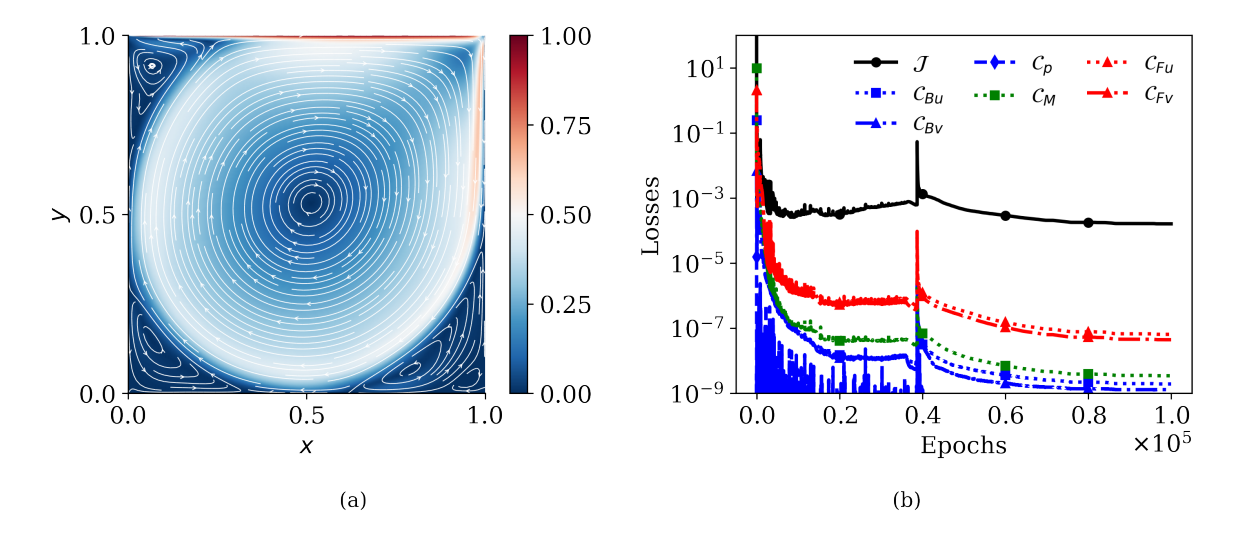


Figure 9: Lid-driven cavity flow at Re = 7500: (a) velocity field with streamlines from one Fourier-network trial with adaptive entropy viscosity; (b) corresponding loss evolution.

The rectangular computational domain contains a cylinder of diameter D=1 centered at the origin, with each boundary located 12D away from the cylinder surface. A total of 30,000 residual points are randomly sampled inside the domain, excluding those within the cylinder, along with 512 points on the cylinder surface and 1,024 points on each boundary. Figure 10 illustrates the distribution of randomly sampled points within the domain and along the boundaries, along with the corresponding boundary conditions.

In Fig. 10, a constant-velocity Dirichlet boundary condition is prescribed at the inlet, where the velocity components  $(u_{po} \text{ and } v_{po})$  are determined from potential flow theory based on a mean unit inflow velocity. The side boundaries employ symmetry (free-slip) conditions, where both the normal velocity and the derivative of the tangential velocity in the normal direction are set to zero. At the outlet, Neumann boundary conditions are applied to the velocity field.

For the pressure field, we consider two treatments: (a) a constant Dirichlet condition (p=0) imposed on the outlet boundary, and (b) a pressure-anchoring strategy in which the pressure is fixed at a single reference point in the bottom-left corner  $(p_{an}=0)$ , leaving open whether a Neumann condition should also be applied at the outlet. In our analysis, we first examine the case with a homogeneous Neumann condition on the outlet for pressure, and then the case in which no Neumann condition is enforced there.

To formulate these cases consistently, the same types of physical quantities are grouped into corresponding constraint terms. Accordingly, two formal optimization formulations are obtained based on the chosen pressure treatment:

$$\min_{\theta} \mathcal{J}(\theta; \boldsymbol{x}), \text{ subject to}$$

$$\mathcal{C}(\theta; \boldsymbol{x}) = [\mathcal{C}_{Fu}, \mathcal{C}_{Fv}, \mathcal{C}_{M}, \mathcal{C}_{Bu}, \mathcal{C}_{Bv}, \mathcal{C}_{Bp}, \mathcal{C}_{Bu_{y}}, \mathcal{C}_{Bu_{x}}, \mathcal{C}_{Bv_{x}}]^{T} = \boldsymbol{0}, \tag{19a}$$

$$\mathcal{C}(\theta; \boldsymbol{x}) = [\mathcal{C}_{Fu}, \mathcal{C}_{Fv}, \mathcal{C}_{M}, \mathcal{C}_{Bu}, \mathcal{C}_{Bv}, \mathcal{C}_{p_{an}}, \mathcal{C}_{Bu_{y}}, \mathcal{C}_{Bu_{x}}, \mathcal{C}_{Bv_{x}}, \mathcal{C}_{Bp_{x}}]^{T} = \boldsymbol{0}. \tag{19b}$$

Here, we employ a simple MLP consisting of three hidden layers with 60 neurons per layer, trained using the L-BFGS optimizer for 20,000 epochs. Figure 11 shows the predicted velocity

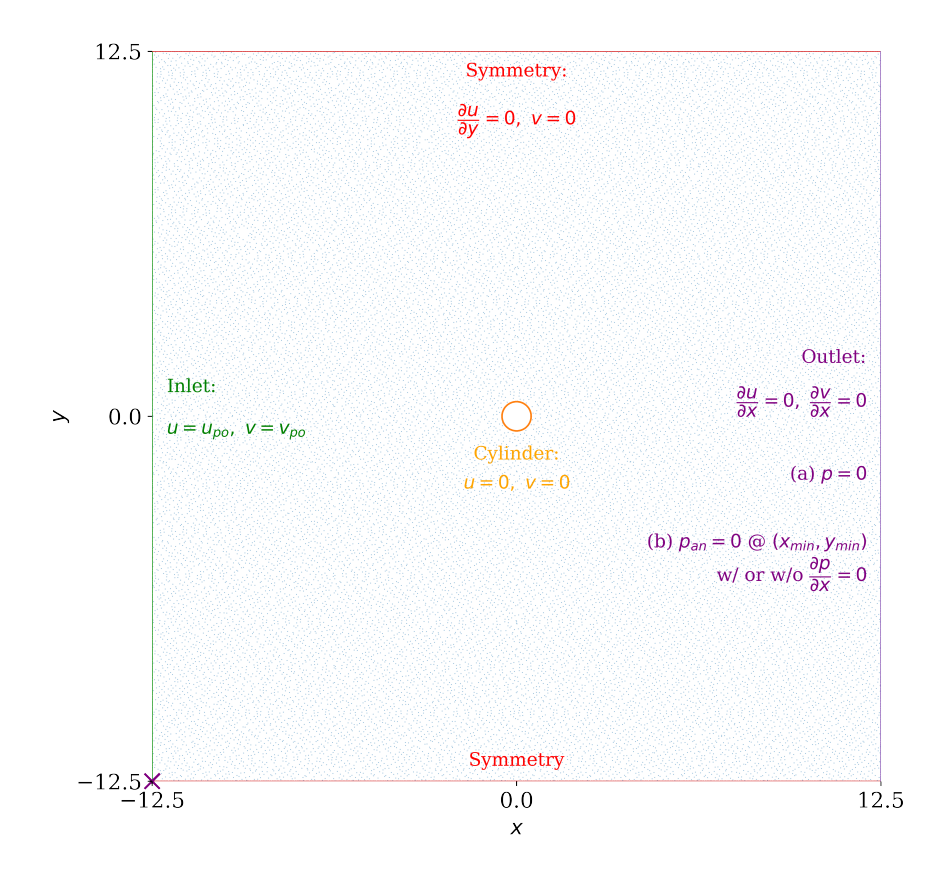


Figure 10: Flow over a cylinder at Re = 40: distribution of randomly sampled residual and boundary points, along with the prescribed boundary conditions. Note that boundary conditions on the pressure field is optional aside from anchoring it at a single arbitrary point in the domain.

and pressure fields obtained from the formulation (19a) with the constant pressure Dirichlet outlet condition, along with the evolution of the corresponding loss terms. Globally, the predicted velocity and pressure fields follow the expected physical behavior, with clear flow obstruction by the cylinder in Figs. 11(a,b). The zoomed-in view in Fig. 11(c) reveals two symmetric attached vortices behind the cylinder. The loss evolution in Fig. 11(d) demonstrates the convergence of all constraint and objective terms, aside from a brief rise in the objective value during early training. Notably, the constraints associated with Neumann boundary conditions, such as the symmetry and outlet velocity, converge first, followed by the Dirichlet conditions and the divergence-free constraint around 10<sup>-7</sup> after approximately 5,000 epochs. The momentum constraints then converge near 10,000 epochs.

However, the direct implementation of formulation (19b), which employs pressure anchoring with a pure Neumann outlet condition for both velocity and pressure, often converges to local minima, as illustrated in Figure 12. A reverse flow with abnormally high velocity magnitude appears near the outlet in Fig. 12(a), accompanied by the corresponding pressure distribution in Fig. 12(b). The phenomenon implies a possible violation of mass conservation, even though the differential form of the divergence-free condition is enforced on all the points. To address this issue, an additional constraint is considered to ensure global conservation of

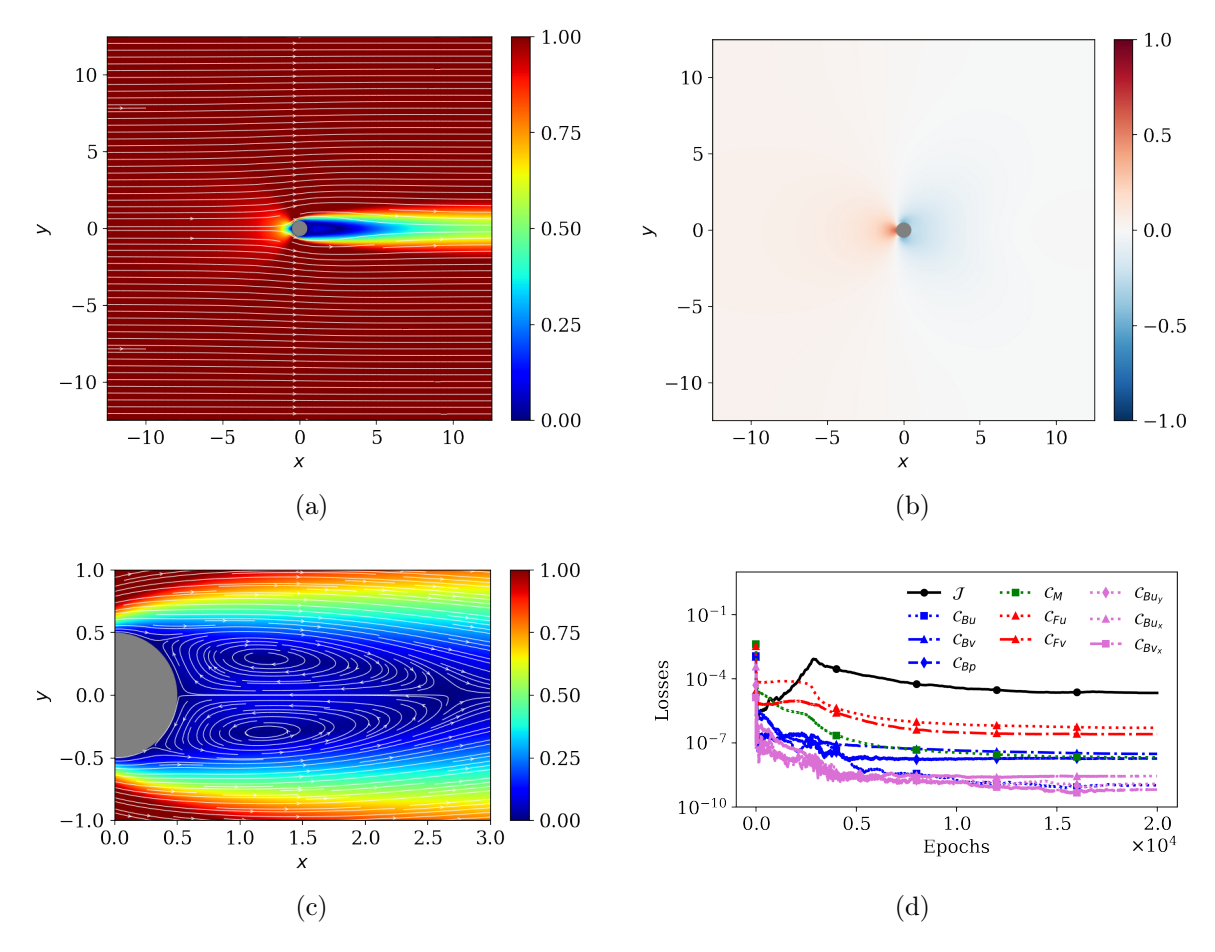


Figure 11: Flow over a cylinder at Re = 40: results of one trial from the formulation (19a) with the constant pressure Dirichlet outlet condition. (a) Global velocity field with streamlines; (b) global pressure distribution; (c) local velocity field in the wake region; (d) corresponding loss evolution.

mass, requiring the incoming mass flow rate to match the outgoing mass flow rate:

$$C_{\dot{m}} = \left\| \frac{1}{N_{\text{out}}} \sum_{i=1}^{N_{\text{out}}} u(x_{\text{max}}, y_i) - \frac{1}{N_{\text{in}}} \sum_{i=1}^{N_{\text{in}}} u_{po}(x_{\text{min}}, y_i) \right\|_{2}^{2} = 0, \tag{20}$$

where  $N_{\text{out}}$  and  $N_{\text{in}}$  denote the numbers of sampled points on the outlet and inlet boundaries, respectively, which are equally-distributed points in this case. This enforcement of global mass conservation by matching the mass flow rate at the inlet and outlet boundaries is a common practice in CFD solvers, when pressure is not specified as a Dirichlet condition at the outflow boundaries.

Figure 13 shows the evolution of loss terms for the same trial presented in Fig. 12, as well as for the formulation (19b) with the additional mass flow rate constraint applied. A clear difference can be observed between the two cases: in Fig. 13(a), the objective function continues to increase gradually throughout training, whereas in Fig. 13(b), it decreases rapidly after an initial rise—the same pattern in Fig. 11(d)—and converges within approximately 5,000 epochs. This improvement results from the explicit enforcement of the net mass flow rate, as

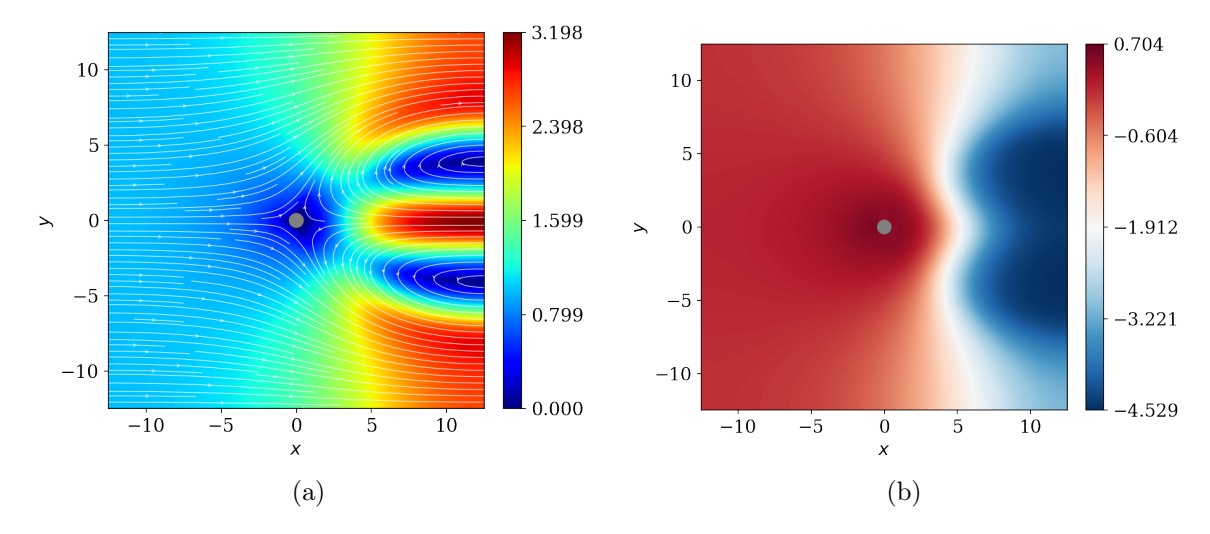


Figure 12: Flow over a cylinder at Re = 40: results of a poorly converged trial from the formulation (19b) with pressure anchoring and pure Neumann outlet condition. (a) Global velocity field with streamlines; (b) global pressure distribution.

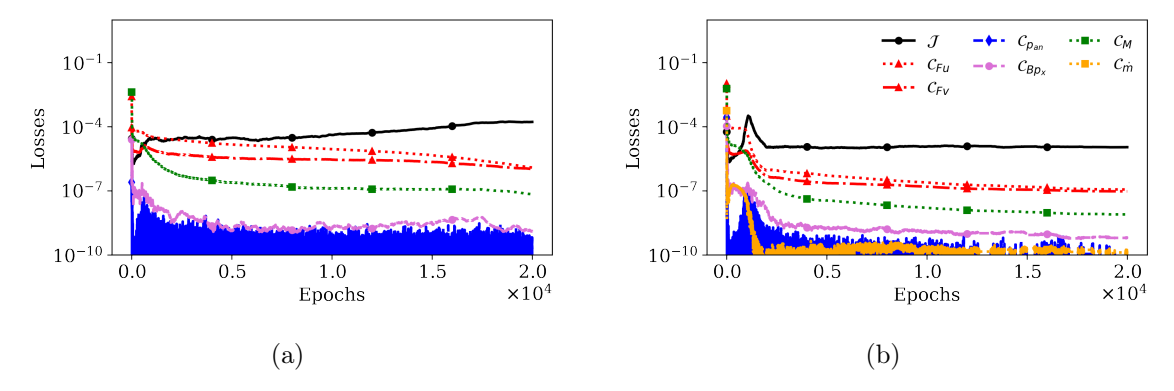


Figure 13: Flow over a cylinder at Re = 40: evolution of loss terms for the formulation (19b) with pressure anchoring and a pure Neumann outlet condition. (a) corresponding to the same trial shown in Fig. 12; (b) with the additional mass flow rate constraint applied.

evidenced by the rapid convergence of the orange curve in Fig. 13(b), which indicates strict satisfaction of the mass balance constraint.

Table 1 summarizes the statistical performance over five independent trials for each formulation: the constant-pressure outlet formulation (19a) and two choices of the pressure-anchoring formulation (19b) with the mass rate constraint  $C_m$ . The comparison is made in terms of the mean and standard deviation of the drag coefficient  $C_D$ , separation angle  $\theta_s$ , and normalized wake length  $L_w/D$ , against conventional numerical results. All formulations yield acceptable difference on the evaluation metrics, compared to the mean value of previous numerical studies. Without any boundary condition on pressure, the pressure-anchoring formulation (19b) with  $C_m$  exhibits the best agreement with reference data, only leaving wake length has ex. This improvement can be attributed to the fact that the pressure-Neumann outlet condition imposes less artificial influence on the near-cylinder flow field compared to the constant-pressure outlet condition.

	$C_D$	$\theta_s$	$L_w/D$
- T			,
Dennis and Chang [38]	1.52	$126.2^{\circ}$	2.35
Fornberg [39]	1.50	$124.4^{\circ}$	2.24
He and Doolen [40]	1.50	$127.2^{\circ}$	2.25
Ye et al. [41]	1.52		2.27
Calhoun [42]	1.62	$125.8^{\circ}$	2.18
Linnick and Fasel [43]	1.54	$126.4^{\circ}$	2.28
Ding et al. [44]	1.58	$127.2^{\circ}$	2.35
Taira and Colonius [45]	1.54	$126.3^{\circ}$	2.30
Patil and Lakshmisha [46]	1.56	$127.3^{\circ}$	2.14
Bouchon et al. [47]	1.50	$126.6^{\circ}$	2.26
Gautier et al. [48]	1.49	$126.4^{\circ}$	2.24
Mean of various works from [48]	$1.53 \pm 0.04$	$126.4^{\circ}\pm0.9^{\circ}$	$2.26 \pm 0.07$
Formulation (19a)	$1.54 \pm 0.01$	$126.9^{\circ} \pm 0.2^{\circ}$	$2.17 \pm 0.001$
Formulation (19b) w/ $\mathcal{C}_{\dot{m}}$	$1.55 \pm 0.004$	$128.0^{\circ}\pm0.8^{\circ}$	$2.22 \pm 0.02$
Formulation (19b) w/ $\mathcal{C}_m$ but w/o $\mathcal{C}_{Bp_x}$	$1.53 \pm 0.01$	$126.2^{\circ}\pm0.7^{\circ}$	$2.23 \pm 0.01$

Table 1: Flow over a cylinder at Re = 40: mean and standard deviation of drag coefficient  $C_D$ , separation angle  $\theta_s$ , and normalized wake length  $L_w/D$ , obtained from the constant-pressure outlet formulation (19a) and the pressure-Neumann outlet formulation (19b) with  $C_{\dot{m}}$ , compared against conventional numerical results.

#### 4. Conclusion

In this work, we have presented a meshless method for simulating incompressible flows using the Navier–Stokes equations in primitive variables (i.e. velocity and pressure). Our method is based on the physics and equality constrained artificial neural networks (PECANN) framework [23], with a single neural network parameterizing both the velocity and pressure fields. The constrained optimization problem, which is central to the PECANN framework, is formulated such that the residual form of the pressure Poisson equation is constrained by the momentum and continuity equations, together with boundary conditions imposed on the velocity field (Eq. 6). Aside from anchoring the pressure at a single arbitrary point in the domain, no explicit boundary conditions on the pressure field are required. Principled enforcement of these constraints is achieved through the recently developed conditionally adaptive augmented Lagrangian method [26]. To further enhance robustness for advection-dominated, high–Reynolds-number flows, we introduced an adaptive, vanishing artificial entropy viscosity that stabilizes the optimization procedure during the early stages of training and decays once it becomes smaller than the physical viscosity.

Ablation studies on the 2D lid-driven cavity flow at Re = 2500 demonstrate that the proposed pressure-based formulation consistently outperforms the baseline formulation that aims to minimize residual form of the momentum equations constrained by the boundary conditions and a divergence-free velocity field condition, even when both are equipped with enhancements such as adaptive entropy viscosity and Fourier feature mapping. Furthermore, with these enhancements, the pressure-based formulation successfully predicts the secondary vortex in the bottom-right corner at Re = 7500.

For the external-flow case of 2D steady flow over a cylinder at Re = 40, the proposed pressure-based method effectively accommodates a general configuration with inflow and outflow boundaries. The resulting drag coefficient, separation angle, and wake length show excellent agreement with established numerical results.

Our method represents neural-network-based meshless solver for incompressible flows, and provide a foundation for future extensions to complex flow problems, including inverse problems involving fluid flow. Because the pressure Poisson equation adopted in our method does not have any temporal derivatives, the proposed formulation has clear potential for unsteady flow problems. As part of future work, we plan to investigate time-dependent flow over a cylinder at Re = 100 without using any numerical data for the initial condition, in order to assess whether vortex shedding can be captured and whether the Strouhal number can be accurately matched.

.

# Acknowledgments

This material is based upon work supported by the National Science Foundation under Grant No. 1953204 and in part by the University of Pittsburgh Center for Research Computing through the resources provided.

# Declaration of generative AI and AI-assisted technologies in the writing

During the preparation of this work the author(s) used Microsoft Copilot and ChatGPT in order to assist with improving the clarity and quality of the English language. After using this tool/service, the author(s) reviewed and edited the content as needed and take(s) full responsibility for the content of the publication.

#### References

- [1] F. H. Harlow, J. E. Welch, Numerical calculation of time-dependent viscous incompressible flow of fluid with free surface, Physics of Fluids 8 (1965) 2182–2189.
- [2] A. J. Chorin, Numerical solution of the navier–stokes equations, Mathematics of Computation 22 (1968) 745–762.
- [3] R. Témam, Sur l'approximation de la solution des équations de Navier-Stokes par la méthode des pas fractionnaires (II), Arch. Rational Mech. Anal. 33 (1969) 377–385.
- [4] A. A. Amsden, F. H. Harlow, A simplified MAC technique for incompressible fluid flow calculations, J. Comput. Phys. 6 (1970) 322–325.
- [5] J. Kim, P. Moin, Application of a fractional-step method to incompressible navier-stokes equations, J. Comput. Phys. 59 (1985) 308–323.
- [6] J. Guermond, P. Minev, J. Shen, An overview of projection methods for incompressible flows, Comput. Methods Appl. Mech. Eng. 195 (2006) 6011–6045.
- [7] S. V. Patankar, D. B. Spalding, A calculation procedure for heat, mass and momentum transfer in three-dimensional parabolic flows, International Journal of Heat and Mass Transfer 15 (1972) 1787–1806.

- [8] S. V. Patankar, A calculation procedure for two-dimensional elliptic situations, Numerical Heat Transfer 4 (1981) 409–425.
- [9] J. P. Van Doormaal, G. D. Raithby, Enhancements of the simple method for predicting incompressible fluid flows, Numerical Heat Transfer 7 (1984) 147–163.
- [10] R. I. Issa, A. D. Gosman, A. P. Watkins, The computation of compressible and incompressible recirculating flows by a noniterative implicit scheme, Journal of Computational Physics 62 (1986) 66–82.
- [11] S. A. Orszag, M. Israeli, M. O. Deville, Boundary conditions for incompressible flows, J. Sci. Comput. 1 (1986) 75–111.
- [12] G. E. Karniadakis, M. Israeli, S. A. Orszag, High-order splitting methods for the incompressible navier-stokes equations, J. Comput. Phys. 97 (1991) 414–443.
- [13] J. L. Guermond, J. Shen, Velocity-correction projection methods for incompressible flows, SIAM J. Numer. Anal. 41 (2003) 112–134.
- [14] C. Cantwell, D. Moxey, A. Comerford, A. Bolis, G. Rocco, G. Mengaldo, D. De Grazia, S. Yakovlev, J.-E. Lombard, D. Ekelschot, B. Jordi, H. Xu, Y. Mohamied, C. Eskilsson, B. Nelson, P. Vos, C. Biotto, R. Kirby, S. Sherwin, Nektar++: An open-source spectral/hp element framework, Comput. Phys. Commun. 192 (2015) 205–219.
- [15] NEK5000: Fast high-order scalable CFD, https://nek5000.mcs.anl.gov/, 2025. Accessed: 22 November 2025.
- [16] X. Jin, S. Cai, H. Li, G. E. Karniadakis, NSFnets (navier-stokes flow nets): Physics-informed neural networks for the incompressible navier-stokes equations 426 (????) 109951.
- [17] H. Eivazi, M. Tahani, P. Schlatter, R. Vinuesa, Physics-informed neural networks for solving reynolds-averaged navier—stokes equations, Phys. Fluids 34 (2022) 075117.
- [18] C. J. McDevitt, E. Fowler, S. Roy, Physics-constrained deep learning of incompressible cavity flows, 2022. URL: https://arxiv.org/abs/2211.06375. arXiv:2211.06375.
- [19] S. Wang, B. Li, Y. Chen, P. Perdikaris, Piratenets: Physics-informed deep learning with residual adaptive networks, Journal of Machine Learning Research 25 (2024) 1–51.
- [20] S. Wang, S. Sankaran, X. Fan, P. Stinis, P. Perdikaris, Simulating three-dimensional turbulence with physics-informed neural networks, 2025. URL: https://arxiv.org/ abs/2507.08972. arXiv:2507.08972.
- [21] S. Wang, S. Sankaran, P. Perdikaris, Respecting causality for training physics-informed neural networks, Comput. Methods Appl. Mech. Eng. 421 (2024) 116813.
- [22] N. Vyas, D. Morwani, R. Zhao, M. Kwun, I. Shapira, D. Brandfonbrener, L. Janson, S. Kakade, Soap: Improving and stabilizing shampoo using adam, 2025. URL: https://arxiv.org/abs/2409.11321. arXiv:2409.11321.

- [23] S. Basir, I. Senocak, Physics and equality constrained artificial neural networks: Application to forward and inverse problems with multi-fidelity data fusion, J. Comput. Phys. 463 (2022) 111301.
- [24] M. R. Hestenes, Multiplier and gradient methods, J. Optim. Theory Appl. 4 (1969) 303–320.
- [25] M. J. Powell, A method for nonlinear constraints in minimization problems, in: R. Fletcher (Ed.), Optimization; Symposium of the Institute of Mathematics and Its Applications, University of Keele, England, 1968, Academic Press, London, New York, 1969, pp. 283–298.
- [26] Q. Hu, S. Basir, I. Senocak, Conditionally adaptive augmented lagrangian method for physics-informed learning of forward and inverse problems using artificial neural networks, 2025. URL: https://arxiv.org/abs/2508.15695. arXiv:2508.15695.
- [27] J.-L. Guermond, R. Pasquetti, B. Popov, Entropy viscosity method for nonlinear conservation law, Journal of Computational Physics 230 (2011) 4248–4267.
- [28] Z. Wang, M. S. Triantafyllou, Y. Constantinides, G. Karniadakis, An entropy-viscosity large eddy simulation study of turbulent flow in a flexible pipe, Journal of Fluid Mechanics 859 (2019) 691–730.
- [29] K. Shukla, J. D. Toscano, Z. Wang, Z. Zou, G. E. Karniadakis, A comprehensive and FAIR comparison between MLP and KAN representations for differential equations and operator networks, Comput. Methods Appl. Mech. Eng. 431 (2024) 117290.
- [30] Y. He, Z. Wang, H. Xiang, X. Jiang, D. Tang, An artificial viscosity augmented physics-informed neural network for incompressible flow, Appl. Math. Mech.-Engl. Ed. 44 (2023) 1101–1110.
- [31] M. Tancik, P. P. Srinivasan, B. Mildenhall, S. Fridovich-Keil, N. Raghavan, U. Singhal, R. Ramamoorthi, J. T. Barron, R. Ng, Fourier features let networks learn high frequency functions in low dimensional domains, in: Proceedings of the 34th International Conference on Neural Information Processing Systems, NIPS '20, Curran Associates Inc., Red Hook, NY, USA, 2020.
- [32] S. Wang, H. Wang, P. Perdikaris, On the eigenvector bias of Fourier feature networks: From regression to solving multi-scale PDEs with physics-informed neural networks, Comput. Methods Appl. Mech. Eng. 384 (2021) 113938.
- [33] X. Glorot, Y. Bengio, Understanding the difficulty of training deep feedforward neural networks, in: Y. W. Teh, M. Titterington (Eds.), Proceedings of the Thirteenth International Conference on Artificial Intelligence and Statistics, volume 9 of *Proceedings of Machine Learning Research*, PMLR, Chia Laguna Resort, Sardinia, Italy, 2010, pp. 249–256.

- [34] A. Paszke, S. Gross, F. Massa, A. Lerer, J. Bradbury, G. Chanan, T. Killeen, Z. Lin, N. Gimelshein, L. Antiga, A. Desmaison, A. Köpf, E. Yang, Z. DeVito, M. Raison, A. Tejani, S. Chilamkurthy, B. Steiner, L. Fang, J. Bai, S. Chintala, PyTorch: An Imperative Style, High-Performance Deep Learning Library, Curran Associates Inc., Red Hook, NY, USA, 2019.
- [35] U. Ghia, K. Ghia, C. Shin, High-re solutions for incompressible flow using the Navier-Stokes equations and a multigrid method, J. Comput. Phys. 48 (1982) 387–411.
- [36] E. Erturk, T. C. Corke, C. Gökçöl, Numerical solutions of 2-d steady incompressible driven cavity flow at high reynolds numbers 48 (????) 747–774.
- [37] R. Gautier, D. Biau, E. Lamballais, A reference solution of the flow over a circular cylinder at re=40 75 (????) 103–111.
- [38] S. C. R. Dennis, G.-Z. Chang, Numerical solutions for steady flow past a circular cylinder at reynolds numbers up to 100, Journal of Fluid Mechanics 42 (1970) 471–489.
- [39] B. Fornberg, A numerical study of steady viscous flow past a circular cylinder, Journal of Fluid Mechanics 98 (1980) 819–855.
- [40] X. He, G. Doolen, Lattice boltzmann method on curvilinear coordinates system: Flow around a circular cylinder, Journal of Computational Physics 134 (1997) 306–315.
- [41] T. Ye, R. Mittal, H. Udaykumar, W. Shyy, An accurate cartesian grid method for viscous incompressible flows with complex immersed boundaries, Journal of Computational Physics 156 (1999) 209–240.
- [42] D. Calhoun, A cartesian grid method for solving the two-dimensional streamfunction-vorticity equations in irregular regions, Journal of computational physics 176 (2002) 231–275.
- [43] M. N. Linnick, H. F. Fasel, A high-order immersed interface method for simulating unsteady incompressible flows on irregular domains, Journal of Computational Physics 204 (2005) 157–192.
- [44] H. Ding, C. Shu, Q. Cai, Applications of stencil-adaptive finite difference method to incompressible viscous flows with curved boundary, Computers & fluids 36 (2007) 786–793.
- [45] K. Taira, T. Colonius, The immersed boundary method: a projection approach, Journal of Computational Physics 225 (2007) 2118–2137.
- [46] D. V. Patil, K. Lakshmisha, Finite volume tvd formulation of lattice boltzmann simulation on unstructured mesh, Journal of Computational Physics 228 (2009) 5262–5279.
- [47] F. Bouchon, T. Dubois, N. James, A second-order cut-cell method for the numerical simulation of 2d flows past obstacles, Computers & Fluids 65 (2012) 80–91.
- [48] R. Gautier, D. Biau, E. Lamballais, A reference solution of the flow over a circular cylinder at re=40, Computers & Fluids 75 (2013) 103–111.